

## 7.11

# MODELING THE DYNAMICS OF DISLOCATION ENSEMBLES

Nasr M. Ghoniem

*Department of Mechanical and Aerospace Engineering, University of California,  
Los Angeles, CA 90095-1597, USA*

### 1. Introduction

A fundamental description of plastic deformation is under development by several research groups as a result of dissatisfaction with the limitations of continuum plasticity theory. The reliability of continuum plasticity descriptions is dependent on the accuracy and range of available experimental data. Under complex loading situations, however, the database is often hard to establish. Moreover, the lack of a characteristic length scale in continuum plasticity makes it difficult to predict the occurrence of critical localized deformation zones. It is widely appreciated that plastic strain is fundamentally heterogeneous, displaying high strains concentrated in small material volumes, with virtually undeformed regions in-between. Experimental observations consistently show that plastic deformation is internally heterogeneous at a number of length scales [1–3]. Depending on the deformation mode, heterogeneous dislocation structures appear with definitive wavelengths. It is common to observe persistent slip bands (PSBs), shear bands, dislocation pile ups, dislocation cells and sub grains. However, a satisfactory description of realistic dislocation patterning and strain localization has been rather elusive. Since dislocations are the basic carriers of plasticity, the fundamental physics of plastic deformation must be described in terms of the behavior of dislocation ensembles. Moreover, the deformation of thin films and nanolayered materials is controlled by the motion and interactions of dislocations. For all these reasons, there has been significant recent interest in the development of robust computational methods to describe the collective motion of dislocation ensembles. Studies of the mechanical behavior of materials at a length scale larger than what can be handled by direct atomistic simulations, and smaller than what allows macroscopic continuum averaging represent particular difficulties. Two

complimentary approaches have been advanced to model the mechanical behavior in this *meso* length scale.

The first approach, commonly known as dislocation dynamics (DD), was initially motivated by the need to understand the origins of heterogeneous plasticity and pattern formation. In its early versions, the collective behavior of dislocation ensembles was determined by direct numerical simulations of the interactions between infinitely long, straight dislocations [3–9]. Recently, several research groups extended the DD methodology to the more physical, yet considerably more complex 3D simulations. Generally, coarse resolution is obtained by the *Lattice Method*, developed by Kubin *et al.* [10] and Moulin *et al.* [11], where straight dislocation segments (either pure screw or edge in the earliest versions, or of a mixed character in more recent versions) are allowed to jump on specific lattice sites and orientations. Straight dislocation segments of mixed character in the *The Force Method*, developed by Hirth *et al.* [12] and Zbib *et al.* [13] are moved in a rigid body fashion along the normal to their mid-points, but they are not tied to an underlying spatial lattice or grid. The advantage of this method is that the explicit information on the elastic field is not necessary, since closed-form solutions for the interaction forces are directly used. *The Differential Stress Method* developed by Schwarz and Tersoff [14] and Schwarz [15] is based on calculations of the stress field of a differential straight line element on the dislocation. Using numerical integration, Peach–Koehler forces on all other segments are determined. The Brown procedure [16] is then utilized to remove the singularities associated with the self-force calculation. The method of *The Phase Field Microelasticity* [17–19] is of a different nature. It is based on Khachaturyan–Shatalov (KS) reciprocal space theory of the strain in an arbitrary elastically homogeneous system of misfitting coherent inclusions embedded into the parent phase. Thus, consideration of individual segments of all dislocation lines is not required. Instead, the temporal and spatial evolution of several density function profiles (fields) are obtained by solving continuum equations in Fourier space.

The second approach to mechanical models at the *mesoscale* has been based on statistical mechanics methods [20–24]. In these developments, evolution equations for statistical averages (and possibly for higher moments) are to be solved for a complete description of the deformation problem. We focus here on the most recent formulations of 3D DD, following the work of Ghoniem *et al.*

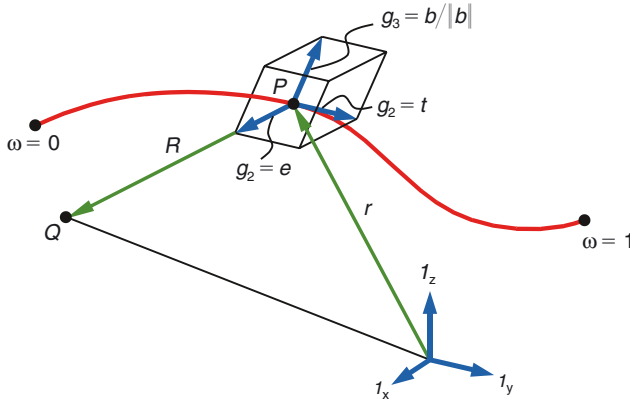
We review here the most recent developments in computational DD for the direct numerical simulation of the interaction and evolution of complex, 3D dislocation ensembles. The treatment is based on the parametric dislocation dynamics (PDD), developed by Ghoniem *et al.* In Section 2, we describe the geometry of dislocation loops with curved, smooth, continuous parametric segments. The stress field of ensembles of such curved dislocation loops is then developed in Section 3. Equations of motion for dislocation loops

are derived on the basis of irreversible thermodynamics, where the time rate of change of generalized coordinates will be given in Section 4. Extensions of these methods to anisotropic materials and multi-layered thin films are discussed in Section 5. Applications of the parametric dislocation dynamics methods are given in Section 6, and a discussion of future directions is finally outlined in Section 7.

## 2. Computational Geometry of Dislocation Loops

Assume that the dislocation line is segmented into  $(n_s)$  arbitrary curved segments, labeled  $(1 \leq i \leq n_s)$ . For each segment, we define  $\hat{\mathbf{r}}(\omega) = \mathbf{P}(\omega)$  as the position vector for any point on the segment,  $\mathbf{T}(\omega) = T\mathbf{t}$  as the tangent vector to the dislocation line, and  $\mathbf{N}(\omega) = N\mathbf{n}$  as the normal vector at any point (see Fig. 1). The space curve is then completely described by the parameter  $\omega$ , if one defines certain relationships which determine  $\hat{\mathbf{r}}(\omega)$ . Note that the position of any other point in the medium (Q) is denoted by its vector  $\mathbf{r}$ , and that the vector connecting the source point  $\mathbf{P}$  to the field point is  $\mathbf{R}$ , thus  $\mathbf{R} = \mathbf{r} - \hat{\mathbf{r}}$ . In the following developments, we restrict the parameter  $0 \leq \omega \leq 1$ , although we map it later on the interval  $-1 \leq \hat{\omega} \leq 1$ , and  $\hat{\omega} = 2\omega - 1$  in the numerical quadrature implementation of the method.

To specify a parametric form for  $\hat{\mathbf{r}}(\omega)$ , we will now choose a set of generalized coordinates  $\mathbf{q}_i^{(j)}$  for each segment  $(j)$ , which can be quite general. If one defines a set of basis functions  $C_i(\omega)$ , where  $\omega$  is a parameter, and allows



Q1

Figure 1. Differential geometry representation of a general parametric curved dislocation segment.

for index sums to extend also over the basis set ( $i = 1, 2, \dots, I$ ), the equation of the segment can be written as

$$\hat{\mathbf{r}}^{(j)}(\omega) = \mathbf{q}_i^{(j)} C_i(\omega) \quad (1)$$

## 2.1. Linear Parametric Segments

The *shape functions* of linear segments  $C_i(\omega)$ , and their derivatives  $C_{i,\omega}$  take the form:  $C_1 = 1 - \omega$ ,  $C_2 = \omega$  and  $C_{1,\omega} = -1$ ,  $C_{2,\omega} = 1$ . Thus, the available degrees of freedom for a *free, or unconnected* linear segment ( $j$ ) are just the position vectors of the beginning ( $j$ ) and end ( $j + 1$ ) nodes.

$$q_{1k}^{(j)} = P_k^{(j)} \quad \text{and} \quad q_{2k}^{(j)} = P_k^{(j+1)} \quad (2)$$

## 2.2. Cubic Spline Parametric Segments

For cubic spline segments, we use the following set of shape functions, their parametric derivatives, and their associated degrees of freedom, respectively:

$$C_1 = 2\omega^3 - 3\omega^2 + 1, \quad C_2 = -2\omega^3 + 3\omega^2, \quad C_3 = \omega^3 - 2\omega^2 + \omega, \\ \text{and} \quad C_4 = \omega^3 - \omega^2 \quad (3)$$

$$C_{1,\omega} = 6\omega^2 - 6\omega, \quad C_{2,\omega} = -6\omega^2 + 6\omega, \quad C_{3,\omega} = 3\omega^2 - 4\omega + 1, \\ \text{and} \quad C_{4,\omega} = 3\omega^2 - 2\omega \quad (4)$$

$$q_{1k}^{(j)} = P_k^{(j)}, \quad q_{2k}^{(j)} = P_k^{(j+1)}, \quad q_{3k}^{(j)} = T_k^{(j)}, \quad \text{and} \quad q_{4k}^{(j)} = T_k^{(j+1)} \quad (5)$$

Extensions of these methods to other parametric shape functions, such as circular, elliptic, helical, and composite quintic space curves are discussed by Ghoniem *et al.* [25].

Forces and energies of dislocation segments are given per unit length of the curved dislocation line. Also, line integrals of the elastic field variables are carried over differential line elements. Thus, if we express the Cartesian differential in the parametric form:  $d\ell_k^{(j)} = \hat{\mathbf{r}}_{k,\omega}^{(j)} d\omega = q_{sk}^{(j)} C_{s,\omega} d\omega$ . The arc length differential for segment  $j$  is then given by

$$|d\ell^{(j)}| = \left( d\ell_k^{(j)} d\ell_k^{(j)} \right)^{1/2} = \left( \hat{\mathbf{r}}_{k,\omega}^{(j)} \hat{\mathbf{r}}_{k,\omega}^{(j)} \right)^{1/2} d\omega \quad (6)$$

$$= \left( q_{pk}^{(j)} C_{p,\omega} q_{sk}^{(j)} C_{s,\omega} \right)^{1/2} d\omega \quad (7)$$

### 3. Elastic Field Variables as Fast Sums

#### 3.1. Formulation

In materials that can be approximated as infinite and elastically isotropic, the displacement vector  $\mathbf{u}$ , strain  $\varepsilon$  and stress  $\sigma$  tensor fields of a closed dislocation loop are given by deWit [26]

$$u_i = -\frac{b_i}{4\pi} \oint_C A_k dl_k + \frac{1}{8\pi} \oint_C \left[ \epsilon_{ikl} b_l R_{,pp} + \frac{1}{1-\nu} \epsilon_{kmn} b_n R_{,mi} \right] dl_k \quad (8)$$

$$\varepsilon_{ij} = \frac{1}{8\pi} \oint_C \left[ -\frac{1}{2} (\epsilon_{jkl} b_l R_{,l} + \epsilon_{ikl} b_j R_{,l} - \epsilon_{ikl} b_l R_{,j} - \epsilon_{jkl} b_l R_{,i})_{,pp} \right. \\ \left. \times \frac{\epsilon_{kmn} b_n R_{,mij}}{1-\nu} \right] dl_k \quad (9)$$

$$\sigma_{ij} = \frac{\mu}{4\pi} \oint_C \left[ \frac{1}{2} R_{,mpp} (\epsilon_{jmn} dl_i + \epsilon_{imn} dl_j) + \frac{1}{1-\nu} \epsilon_{kmn} \right. \\ \left. \times (R_{,ijm} - \delta_{ij} R_{,ppm}) dl_k \right] \quad (10)$$

where  $\mu$  and  $\nu$  are the shear modulus and Poisson's ratio, respectively,  $\mathbf{b}$  is Burgers vector of Cartesian components  $b_i$ , and the vector potential  $A_k(\mathbf{R}) = \epsilon_{ijk} X_i s_j / [R(R + \mathbf{R} \cdot \mathbf{s})]$  satisfies the differential equation:  $\epsilon_{pik} A_{k,p}(\mathbf{R}) = X_i R^{-3}$ , where  $\mathbf{s}$  is an arbitrary unit vector. The radius vector  $\mathbf{R}$  connects a source point on the loop to a field point, as shown in Fig. 1, with Cartesian components  $R_i$ , successive partial derivatives  $R_{,ijk\dots}$ , and magnitude  $R$ . The line integrals are carried along the closed contour  $C$  defining the dislocation loop, of differential arc length  $dl$  of components  $dl_k$ . Also, the interaction energy between two closed loops with Burgers vectors  $\mathbf{b}_1$  and  $\mathbf{b}_2$ , respectively, can be written as

$$E_I = -\frac{\mu b_{1i} b_{2j}}{8\pi} \oint_{C^{(1)}} \oint_{C^{(2)}} \left[ R_{,kk} \left( dl_{2j} dl_{1i} + \frac{2\nu}{1-\nu} dl_{2i} dl_{1j} \right) \right. \\ \left. + \frac{2}{1-\nu} (R_{,ij} - \delta_{ij} R_{,ll}) dl_{2k} dl_{1k} \right] \quad (11)$$

The higher order derivatives of the radius vector,  $R_{,ij}$  and  $R_{,ijk}$  are components of second and third order Cartesian tensors that are explicitly known [27]. The dislocation segment in Fig. 1 is fully determined as an affine mapping on the scalar interval  $\in [0, 1]$ , if we introduce the tangent vector  $\mathbf{T}$ ,

the unit tangent vector  $\mathbf{t}$ , the unit radius vector  $\mathbf{e}$ , and the vector potential  $\mathbf{A}$ , as follows

$$\mathbf{T} = \frac{d\mathbf{l}}{d\omega}, \quad \mathbf{t} = \frac{\mathbf{T}}{|\mathbf{T}|}, \quad \mathbf{e} = \frac{\mathbf{R}}{R}, \quad \mathbf{A} = \frac{\mathbf{e} \times \mathbf{s}}{R(1 + \mathbf{e} \cdot \mathbf{s})}$$

Let the Cartesian orthonormal basis set be denoted by  $\mathbf{1} \equiv \{\mathbf{1}_x, \mathbf{1}_y, \mathbf{1}_z\}$ ,  $\mathbf{I} = \mathbf{1} \otimes \mathbf{1}$  as the second order unit tensor, and  $\otimes$  denotes tensor product. Now define the three vectors ( $\mathbf{g}_1 = \mathbf{e}$ ,  $\mathbf{g}_2 = \mathbf{t}$ ,  $\mathbf{g}_3 = \mathbf{b}/|\mathbf{b}|$ ) as a covariant basis set for the curvilinear segment, and their contravariant reciprocals as:  $\mathbf{g}^i \cdot \mathbf{g}_j = \delta_j^i$ , where  $\delta_j^i$  is the mixed Kronecker delta and  $V = (\mathbf{g}_1 \times \mathbf{g}_2) \cdot \mathbf{g}_3$  the volume spanned by the vector basis, as shown in Fig. 1. When the previous relationships are substituted into the differential forms of Eqs. (8), (10), with  $V_1 = (\mathbf{s} \times \mathbf{g}_1) \cdot \mathbf{g}_2$ , and  $\mathbf{s}$  an arbitrary unit vector, we obtain the differential relationships (see Ref. [27] for details)

$$\begin{aligned} \frac{du}{d\omega} &= \frac{|\mathbf{b}||\mathbf{T}|V}{8\pi(1-\nu)R} \left\{ \left[ \frac{(1-\nu)V_1/V}{1 + \mathbf{s} \cdot \mathbf{g}_1} \right] \mathbf{g}_3 + (1-2\nu)\mathbf{g}^1 + \mathbf{g}_1 \right\} \\ \frac{d\epsilon}{d\omega} &= -\frac{V|\mathbf{T}|}{8\pi(1-\nu)R^2} \left\{ -\nu (\mathbf{g}^1 \otimes \mathbf{g}_1 + \mathbf{g}_1 \otimes \mathbf{g}^1) \right. \\ &\quad \left. + (1-\nu) (\mathbf{g}^3 \otimes \mathbf{g}_3 + \mathbf{g}_3 \otimes \mathbf{g}^3) + (3\mathbf{g}_1 \otimes \mathbf{g}_1 - \mathbf{I}) \right\} \\ \frac{d\sigma}{d\omega} &= \frac{\mu V|\mathbf{T}|}{4\pi(1-\nu)R^2} \left\{ (\mathbf{g}^1 \otimes \mathbf{g}_1 + \mathbf{g}_1 \otimes \mathbf{g}^1) \right. \\ &\quad \left. + (1-\nu) (\mathbf{g}^2 \otimes \mathbf{g}_2 + \mathbf{g}_2 \otimes \mathbf{g}^2) - (3\mathbf{g}_1 \otimes \mathbf{g}_1 + \mathbf{I}) \right\} \\ \frac{d^2 E_I}{d\omega_1 d\omega_2} &= -\frac{\mu |\mathbf{T}_1| |\mathbf{b}_1| |\mathbf{T}_2| |\mathbf{b}_2|}{4\pi(1-\nu)R} \left\{ (1-\nu) (\mathbf{g}_2^I \cdot \mathbf{g}_3^I) (\mathbf{g}_2^{II} \cdot \mathbf{g}_3^{II}) \right. \\ &\quad \left. + 2\nu (\mathbf{g}_2^{II} \cdot \mathbf{g}_3^I) (\mathbf{g}_2^I \cdot \mathbf{g}_3^{II}) - (\mathbf{g}_2^I \cdot \mathbf{g}_2^{II}) [(\mathbf{g}_3^I \cdot \mathbf{g}_3^{II}) \right. \\ &\quad \left. + (\mathbf{g}_3^I \cdot \mathbf{g}_1) (\mathbf{g}_3^{II} \cdot \mathbf{g}_1)] \right\} \\ \frac{d^2 E_S}{d\omega_1 d\omega_2} &= -\frac{\mu |\mathbf{T}_1| |\mathbf{T}_2| |\mathbf{b}|^2}{8\pi R (1-\nu)} \left\{ (1+\nu) (\mathbf{g}_3 \cdot \mathbf{g}_2^I) (\mathbf{g}_3 \cdot \mathbf{g}_2^{II}) \right. \\ &\quad \left. - [1 + (\mathbf{g}_3 \cdot \mathbf{g}_1)^2] (\mathbf{g}_2^I \cdot \mathbf{g}_2^{II}) \right\} \end{aligned} \quad (12)$$

The superscripts  $I$  and  $II$  in the energy equations are for loops  $I$  and  $II$ , respectively, and  $\mathbf{g}_1$  is the unit vector along the line connecting two interacting points on the loops. The self energy is obtained by taking the limit of 1/2 the interaction energy of two identical loops, separated by the core distance. Note that the interaction energy of prismatic loops would be simple, because  $\mathbf{g}_3 \cdot \mathbf{g}_2 = 0$ . The field equations are affine transformation mappings of the scalar interval neighborhood  $d\omega$  to the vector ( $d\mathbf{u}$ ) and second order tensor ( $d\epsilon$ ,  $d\sigma$ )

neighborhoods, respectively. The maps are given by covariant, contravariant and mixed vector, and tensor functions.

### 3.2. Analytical Solutions

In some simple geometry of Volterra-type dislocations, special relations between  $\mathbf{b}$ ,  $\mathbf{e}$ , and  $\mathbf{t}$  can be obtained, and the entire dislocation line can also be described by one single parameter. In such cases, one can obtain the elastic field by proper choice of the coordinate system, followed by straight-forward integration. Solution variables for the stress fields of infinitely-long pure and edge dislocations are given in Table 1, while those for the stress field along the  $\mathbf{1}_z$ -direction for circular prismatic and shear loops are shown in Table 2. Note that for the case of a pure screw dislocation, one has to consider the product of  $V$  and the contravariant vectors together, since  $V = 0$ . When the parametric equations are integrated over  $z$  from  $-\infty$  to  $+\infty$  for the straight dislocations, and over  $\theta$  from 0 to  $2\pi$  for circular dislocations, one obtains the entire stress field in dyadic notation as:

#### 1. Infinitely-long screw dislocation

$$\sigma = \frac{\mu b}{2\pi r} \left\{ -\sin\theta \mathbf{1}_x \otimes \mathbf{1}_z + \cos\theta \mathbf{1}_y \otimes \mathbf{1}_z + \cos\theta \mathbf{1}_z \otimes \mathbf{1}_y - \sin\theta \mathbf{1}_z \otimes \mathbf{1}_x \right\} \quad (13)$$

Table 1. Variables for screw and edge dislocations

	Screw dislocation	Edge dislocation
$\mathbf{g}_1$	$\frac{1}{R}(r \cos\theta \mathbf{1}_x + r \sin\theta \mathbf{1}_y + z \mathbf{1}_z)$	$\frac{1}{R}(r \cos\theta \mathbf{1}_x + r \sin\theta \mathbf{1}_y + z \mathbf{1}_z)$
$\mathbf{g}_2$	$\mathbf{1}_z$	$\mathbf{1}_z$
$\mathbf{g}_3$	$\mathbf{1}_z$	$\mathbf{1}_x$
$\mathbf{g}^1$	0	$\frac{1}{V} \mathbf{1}_y$
$\mathbf{g}^2$	$\frac{r}{V \sqrt{r^2 + z^2}} (-\sin\theta \mathbf{1}_x + \cos\theta \mathbf{1}_y)$	$\frac{1}{V \sqrt{r^2 + z^2}} (-z \mathbf{1}_y + r \sin\theta \mathbf{1}_z)$
$\mathbf{g}^3$	$\frac{r}{V \sqrt{r^2 + z^2}} (\sin\theta \mathbf{1}_x - \cos\theta \mathbf{1}_y)$	$\frac{r}{V \sqrt{r^2 + z^2}} (\sin\theta \mathbf{1}_x - \cos\theta \mathbf{1}_y)$
$\mathbf{T}$	$\frac{dz}{d\omega} \mathbf{1}_z$	$\frac{dz}{d\omega} \mathbf{1}_z$
$\mathbf{R}$	$\sqrt{r^2 + z^2}$	$\sqrt{r^2 + z^2}$
$\mathbf{V}$	0	$\frac{r \sin\theta}{\sqrt{r^2 + z^2}}$

Table 2. Variables for circular shear and prismatic loops

	Shear loop	Prismatic loop
$\mathbf{g}_1$	$\frac{1}{\sqrt{r^2 + z^2}}(r \cos \theta \mathbf{1}_x + r \sin \theta \mathbf{1}_y + z \mathbf{1}_z)$	$\frac{1}{\sqrt{r^2 + z^2}}(r \cos \theta \mathbf{1}_x + r \sin \theta \mathbf{1}_y + z \mathbf{1}_z)$
$\mathbf{g}_2$	$-\sin \theta \mathbf{1}_x + \cos \theta \mathbf{1}_y$	$-\sin \theta \mathbf{1}_x + \cos \theta \mathbf{1}_y$
$\mathbf{g}_3$	$\mathbf{1}_x$	$\mathbf{1}_z$
$\mathbf{g}^1$	$-\frac{\cos \theta}{V} \mathbf{1}_y$	$\frac{1}{V}(\cos \theta \mathbf{1}_x + \sin \theta \mathbf{1}_y)$
$\mathbf{g}^2$	$\frac{1}{V \sqrt{r^2 + z^2}}(-z \mathbf{1}_y + r \sin \theta \mathbf{1}_z)$	$\frac{r}{V \sqrt{r^2 + z^2}}(-\sin \theta \mathbf{1}_x + \cos \theta \mathbf{1}_y)$
$\mathbf{g}^3$	$\frac{1}{V \sqrt{r^2 + z^2}}(-z \cos \theta \mathbf{1}_x - z \sin \theta \mathbf{1}_y + r \mathbf{1}_z)$	$\frac{1}{V \sqrt{r^2 + z^2}}(-z \cos \theta \mathbf{1}_x - z \sin \theta \mathbf{1}_y + r \mathbf{1}_z)$
$\mathbf{T}$	$-r \sin \theta \frac{d\theta}{d\omega} \mathbf{1}_x + r \cos \theta \frac{d\theta}{d\omega} \mathbf{1}_y$	$-r \sin \theta \frac{d\theta}{d\omega} \mathbf{1}_x + r \cos \theta \frac{d\theta}{d\omega} \mathbf{1}_y$
$\mathbf{R}$	$\sqrt{r^2 + z^2}$	$\sqrt{r^2 + z^2}$
$\mathbf{V}$	$-\frac{z \cos \theta}{\sqrt{r^2 + z^2}}$	$\frac{r}{\sqrt{r^2 + z^2}}$

## 2. Infinitely-long edge dislocation

$$\begin{aligned} \sigma = & -\frac{\mu b}{2\pi(1-\nu)r} \left\{ \sin \theta (2 + \cos 2\theta) \mathbf{1}_x \otimes \mathbf{1}_x - (\sin \theta \cos 2\theta) \mathbf{1}_y \otimes \mathbf{1}_y \right. \\ & \left. + (2\nu \sin \theta) \mathbf{1}_z \otimes \mathbf{1}_z - (\cos \theta \cos 2\theta) (\mathbf{1}_x \otimes \mathbf{1}_y + \mathbf{1}_y \otimes \mathbf{1}_x) \right\} \end{aligned} \quad (14)$$

## 3. Circular shear loop (evaluated on the $\mathbf{1}_z$ -axis)

$$\begin{aligned} \sigma = & \frac{\mu b r^2}{4(1-\nu)(r^2 + z^2)^{5/2}} \left[ (\nu - 2)(r^2 + z^2) + 3z^2 \right] \\ & \times [\mathbf{1}_x \otimes \mathbf{1}_z + \mathbf{1}_z \otimes \mathbf{1}_x] \end{aligned} \quad (15)$$

## 4. Circular prismatic loop (evaluated on the $\mathbf{1}_z$ -axis)

$$\begin{aligned} \sigma = & \frac{\mu b r^2}{4(1-\nu)(r^2 + z^2)^{5/2}} \left\{ (2(1-\nu)(r^2 + z^2) - 3r^2) \right. \\ & \left. \times [\mathbf{1}_x \otimes \mathbf{1}_x + \mathbf{1}_y \otimes \mathbf{1}_y] - 2(4z^2 + r^2) [\mathbf{1}_z \otimes \mathbf{1}_z] \right\} \end{aligned} \quad (16)$$

As an application of the method in calculations of self- and interaction energy between dislocations, we consider here two simple cases. First, the

interaction energy between two parallel screw dislocations of length  $L$  and with a minimum distance  $\rho$  between them is obtained by making the following substitutions in Eq. (12)

$$\mathbf{g}_2^I = \mathbf{g}_2^{II} = \mathbf{g}_3^I = \mathbf{g}_3^{II} = \mathbf{1}_z, \quad |\mathbf{T}| = \frac{dl}{dz} = 1, \quad \mathbf{1}_z \cdot \mathbf{g}_1 = \frac{z_2 - z_1}{\sqrt{\rho^2 + (z_2 - z_1)^2}}$$

where  $z_1$  and  $z_2$  are distances along  $\mathbf{1}_z$  on dislocations 1 and 2, respectively, connected along the unit vector  $\mathbf{g}_1$ . The resulting scalar differential equation for the interaction energy is

$$\frac{d^2 E_I}{dz_1 dz_2} = -\frac{\mu b^2}{4\pi(1-\nu)} \left\{ \frac{\nu}{\sqrt{\rho^2 + (z_2 - z_1)^2}} - \frac{(z_2 - z_1)^2}{[\rho^2 + (z_2 - z_1)^2]^{3/2}} \right\} \quad (17)$$

Integration of Eq. (17) over a finite length  $L$  yields identical results to those obtained by deWit [26] and by application of the more standard Blin formula [28]. Second, the interaction energy between two coaxial prismatic circular dislocations with equal radius can be easily obtained by the following substitutions

$$\mathbf{g}_3^I = \mathbf{g}_3^{II} = \mathbf{1}_z, \quad \mathbf{g}_2^I = -\sin \varphi_1 \mathbf{1}_x + \cos \varphi_1 \mathbf{1}_y, \quad \mathbf{g}_2^{II} = -\sin \varphi_2 \mathbf{1}_x + \cos \varphi_2 \mathbf{1}_y, \\ \mathbf{1}_z \cdot \mathbf{g}_2^I = 0, \quad R^2 = z^2 + (2\rho \sin \frac{\varphi_1 - \varphi_2}{2})^2, \quad \mathbf{1}_z \cdot \mathbf{g}_1 = \frac{z}{R}$$

Integration over the variables  $\varphi_1$  and  $\varphi_2$  from  $(0 - 2\pi)$  yields the interaction energy.

#### 4. Dislocation Loop Motion

Consider the virtual motion of a dislocation loop. The mechanical power during this motion is composed of two parts: (1) change in the elastic energy stored in the medium upon loop motion under the influence of its own stress (i.e., the change in the loop self-energy), (2) the work done on moving the loop as a result of the action of external and internal stresses, excluding the stress contribution of the loop itself. These two components constitute the Peach–Koehler work [29]. The main idea of DD is to derive approximate equations of motion from the principle of Virtual Power Dissipation of the second law of thermodynamics Ghoniem *et al.* [27]. Once the parametric curve for the dislocation segment is mapped onto the scalar interval  $\{\omega \in [0, 1]\}$ , the stress field everywhere is obtained as a fast numerical quadrature sum [30]. The Peach–Koehler force exerted on any other dislocation segment can be obtained from the total stress field (external and internal) at the segment as [30].

$$\mathbf{F}_{PK} = \sigma \cdot \mathbf{b} \times \mathbf{t}.$$

The total self-energy of the dislocation loop is determined by double line integrals. However, Gavazza and Barnett [31] have shown that the first variation in the self-energy of the loop can be written as a single line integral, and that the majority of the contribution is governed by the local line curvature. Based on these methods for evaluations of the interaction and self-forces, the weak variational form of the governing equation of motion of a single dislocation loop was developed by Ghoniem *et al.* [25] as

$$\int_{\Gamma} (F_k^t - B_{ak} V_a) \delta r_k |ds| = 0 \quad (18)$$

Here,  $F_k^t$  are the components of the resultant force, consisting of the Peach–Koehler force  $\mathbf{F}_{PK}$  (generated by the sum of the external and internal stress fields), the self-force  $\mathbf{F}_s$ , and the Osmotic force  $\mathbf{F}_O$  (in case climb is also considered [25]). The resistivity matrix (inverse mobility) is  $B_{ak}$ ,  $V_a$  are the velocity vector components, and the line integral is carried along the arc length of the dislocation  $ds$ . To simplify the problem, let us define the following dimensionless parameters

$$\mathbf{r}^* = \frac{\mathbf{r}}{a}, \quad \mathbf{f}^* = \frac{\mathbf{F}}{\mu a}, \quad t^* = \frac{\mu t}{B}$$

Here,  $a$  is lattice constant, and  $t$  is time. Hence Eq. (18) can be rewritten in dimensionless matrix form as

$$\int_{\Gamma^*} \delta \mathbf{r}^{*\top} \left( \mathbf{f}^* - \frac{d\mathbf{r}^*}{dt^*} \right) |ds^*| = 0 \quad (19)$$

Here,  $\mathbf{f}^* = [f_1^*, f_2^*, f_3^*]^\top$  and  $\mathbf{r}^* = [r_1^*, r_2^*, r_3^*]^\top$ , which are all dependent on the dimensionless time  $t^*$ . Following Ghoniem *et al.* [25], a closed dislocation loop can be divided into  $N_s$  segments. In each segment  $j$ , we can choose a set of generalized coordinates  $q_m$  at the two ends, thus allowing parametrization of the form

$$\mathbf{r}^* = \mathbf{C}\mathbf{Q} \quad (20)$$

Here,  $\mathbf{C} = [C_1(\omega), C_2(\omega), \dots, C_m(\omega)]$ ,  $C_i(\omega)$ , ( $i = 1, 2, \dots, m$ ) are shape functions dependent on the parameter ( $0 \leq \omega \leq 1$ ) and  $\mathbf{Q} = [q_1, q_2, \dots, q_m]^\top$ ,  $q_i$  are a set of generalized coordinates. Substituting Eq. (20) into Eq. (19), we obtain

$$\sum_{j=1}^{N_s} \int_{\Gamma_j} \delta \mathbf{Q}^\top \left( \mathbf{C}^\top \mathbf{f}^* - \mathbf{C}^\top \mathbf{C} \frac{d\mathbf{Q}}{dt^*} \right) |ds| = 0 \quad (21)$$

Let,

$$\mathbf{f}_j = \int_{\Gamma_j} \mathbf{C}^\top \mathbf{f}^* |ds|, \quad \mathbf{k}_j = \int_{\Gamma_j} \mathbf{C}^\top \mathbf{C} |ds|$$

Following a similar procedure to the FEM, we assemble the EOM for all contiguous segments in global matrices and vectors, as

$$\mathbf{F} = \sum_{j=1}^{N_s} \mathbf{f}_j, \quad \mathbf{K} = \sum_{j=1}^{N_s} \mathbf{k}_j$$

then, from Eq. (21) we get,

$$\mathbf{K} \frac{d\mathbf{Q}}{dt^*} = \mathbf{F} \quad (22)$$

The solution of the set of ordinary differential Eq. (22) describes the motion of an ensemble of dislocation loops as an evolutionary dynamical system. However, additional *protocols* or algorithms are used to treat: (1) strong dislocation interactions (e.g., junctions or tight dipoles), (2) dislocation generation and annihilation, (3) adaptive meshing as dictated by large curvature variations [25].

In the *The Parametric Method* [25, 27, 32, 33] presented above, the dislocation loop can be geometrically represented as a continuous (to second derivative) composite space curve. This has two advantages: (1) there is no abrupt variation or singularities associated with the self-force at the joining nodes in between segments, (2) very drastic variations in dislocation curvature can be easily handled without excessive re-meshing.

## 5. Dislocation Dynamics in Anisotropic Crystals

Extension of the PDD to anisotropic linearly elastic crystals follows the same procedure described above, with the exception of two aspects [34]. First, calculations of the elastic field, and hence forces on dislocations, is computationally more demanding. Second, the dislocation self-force is obtained from non-local line integrals. Thus PDD simulations in anisotropic materials are about an order of magnitude slower than in isotropic materials.

Mura [35] derived a line integral expression for the elastic distortion of a dislocation loop, as

$$u_{i,j}(\mathbf{x}) = \epsilon_{jnk} C_{pqmn} b_m \int_L G_{ip,q}(\mathbf{x} - \mathbf{x}') v_k dl(\mathbf{x}'), \quad (23)$$

where  $v_k$  is the unit tangent vector of the dislocation loop line  $L$ ,  $dl$  is the dislocation line element,  $\epsilon_{jnh}$  is the permutation tensor,  $C_{ijkl}$  is the fourth order elastic constants tensor,  $G_{ij,l}(\mathbf{x} - \mathbf{x}') = \partial G_{ij}(\mathbf{x} - \mathbf{x}') / \partial x_l$ , and  $G_{ij}(\mathbf{x} - \mathbf{x}')$  are the Green's tensor functions, which correspond to displacement component along the  $x_i$ -direction at point  $\mathbf{x}$  due to a unit point force in the  $x_j$ -direction applied at point  $\mathbf{x}'$  in an infinite medium.

The elastic distortion formula (23) involves derivatives of the Green's functions, which need special consideration. For general anisotropic solids, analytical expressions for  $G_{ij,k}$  are not available. However, these functions can be expressed in an integral form (see, e.g., Refs. [36–39]), as

$$G_{ij,k}(\mathbf{x} - \mathbf{x}') = \frac{1}{8\pi^2|\mathbf{r}|^2} \oint_{C_k} \left[ -\bar{r}_k N_{ij}(\bar{\mathbf{k}}) D^{-1}(\bar{\mathbf{k}}) + \bar{k}_k C_{lpmq} (\bar{r}_p \bar{k}_q + \bar{k}_p \bar{r}_q) N_{il}(\bar{\mathbf{k}}) N_{jm}(\bar{\mathbf{k}}) D^{-2}(\bar{\mathbf{k}}) \right] d\phi \quad (24)$$

where  $\mathbf{r} = \mathbf{x} - \mathbf{x}'$ ,  $\bar{\mathbf{r}} = \mathbf{r}/|\mathbf{r}|$ ,  $\bar{\mathbf{k}}$  is the unit vector on the plane normal to  $\mathbf{r}$ , the integral is taken around the unit circle  $C_k$  on the plane normal to  $\mathbf{r}$ ,  $N_{ij}(\mathbf{k})$  and  $D(\mathbf{k})$  are the adjoint matrix and the determinant of the second order tensor  $C_{ijkl}k_k k_l$ , respectively.

The in-plane self-force at the point  $P$  on the loop is also obtained in a manner similar to the external Peach–Koehler force, with an additional contribution from *stretching* the dislocation line upon a virtual infinitesimal motion [40]

$$F^S = \kappa E(\mathbf{t}) - \mathbf{b} \cdot \bar{\sigma}^S \cdot \mathbf{n} \quad (25)$$

where  $E(\mathbf{t})$  is the pre-logarithmic energy factor for an infinite straight dislocation parallel to  $\mathbf{t}$ :  $E(\mathbf{t}) = \frac{1}{2} \mathbf{b} \cdot \Sigma(\mathbf{t}) \cdot \mathbf{n}$ , with  $\Sigma(\mathbf{t})$  being the stress tensor of an infinite straight dislocation along the loop's tangent at  $\mathbf{P}$ .  $\sigma^S$  is self stress tensor due to the dislocation  $L$ , and  $\bar{\sigma} = \frac{1}{2} [\sigma^S(\mathbf{P} + \epsilon \mathbf{m}) + \sigma^S(\mathbf{P} - \epsilon \mathbf{m})]$  is the *average* self-stress at  $\mathbf{P}$ ,  $\kappa$  is the in-plane curvature at  $\mathbf{P}$ , and  $\epsilon = |\mathbf{b}|/2$ .

Barnett [40] and Gavazza and Barnett [31] analyzed the structure of the self-force as a sum

$$F^S = \kappa E(\mathbf{t}) - \kappa \left[ E(\mathbf{t}) + E''(\mathbf{t}) \ln \left( \frac{8}{\epsilon \kappa} \right) \right] - J(L, \mathbf{P}) + F_{\text{core}} \quad (26)$$

where the second and third terms are line tension contributions, which usually account for the main part of the self-force, while  $J(L, \mathbf{P})$  is a non-local contribution from other parts of the loop, and  $F_{\text{core}}$  is due to the contribution to the self-energy from the dislocation core.

## 6. Selected Applications

Figure 2 shows the results of computer simulations of plastic deformation in single crystal copper (approximated as elastically isotropic) at a constant strain rate of  $100 \text{ s}^{-1}$ . The initial dislocation density of  $\rho = 2 \times 10^{13} \text{ m}^{-2}$  has been divided into 300 complete loops. Each loop contains a random number

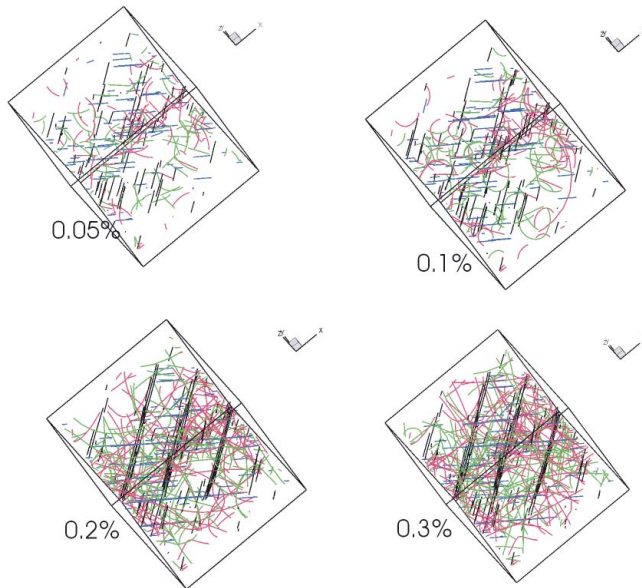


Figure 2. Results of computer simulations for dislocation microstructure deformation in copper deformed to increasing levels of strain (shown next to each microstructure).

of initially straight glide and superjog segments. When a generated or expanding loop intersects the simulation volume of  $2.2\ \mu\text{m}$  side length, the segments that lie outside the simulation boundary are periodically mapped inside the simulation volume to preserve translational strain invariance, without loss of dislocation lines. The number of nodes on each loop starts at five, and is then increased adaptively proportional to the loop length, with a maximum number of 20 nodes per loop. The total number of Degrees of Freedom (DOF) starts at 6000, and is increased to 24 000 by the end of the calculation. However, the number of *interacting* DOF is determined by a nearest neighbor criterion, within a distance of  $400a$  (where  $a$  is the lattice constant), and is based on a binary tree search. The dislocation microstructure is shown in Fig. 2 at different total strain. It is observed that fine slip lines that nucleate at low strains evolve into more pronounced slip bundles at higher strains. The slip bundles are well-separated in space forming a regular pattern with a wavelength of approximately one micron. Conjugate slip is also observed, leading to the formation of dislocation junction bundles and stabilization of a cellular structures.

Next, we consider the dynamic process of dislocation dipole formation in anisotropic single crystals. To measure the degree of deviation from elastic isotropy, we use the *anisotropy ratio*  $A$ , defined in the usual manner:  $A = 2C_{44}/(C_{11} - C_{12})$  [28]. For an isotropic crystal,  $A = 1$ . Figure 3(a) shows the configurations (2D projected on the (111)-plane) of two pinned dislocation segments, lying on parallel (111)-planes. The two dislocation segments are

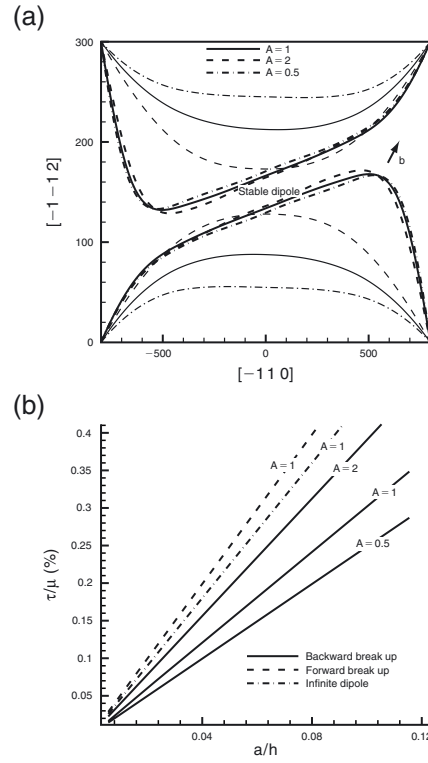


Figure 3. Evolution of dislocation dipoles without applied loading (a) and dipole break up shear stress (b).

initially straight, parallel, and along  $[\bar{1}10]$ , but of opposite line directions, have the same Burgers vector  $\mathbf{b} = 1/2[\bar{1}01]$ , and are pinned at both ends. Their glide planes are separated by  $h$ . In this figure,  $h = 25\sqrt{3}a$ ,  $L : d : h = 800 : 300 : 25\sqrt{3}$ , with  $L$  and  $d$  being the length of the initial dislocation segments and the horizontal distance between them, respectively. Without the application of any external loading, the two lines attract one another, and form an equilibrium state of a finite-size dipole. The dynamic shape of the segments during the dipole formation is seen to be dependent on the anisotropy ratio  $A$ , while the final configuration appears to be insensitive to  $A$ . Under external loading, the dipole may be unzipped, if applied forces overcome binding forces between dipole arms. The forces (resolved shear stresses  $\tau$ , divided by  $\mu = (C_{11} - C_{12})/2$ ) to break up the dipoles are shown in Fig. 3(b). It can be seen that the break up stress is inversely proportional to the separation distance  $h$ , consistent with the results of infinite-size dipoles. It is easier to break up dipoles in crystals with smaller  $A$ -ratios (e.g., some BCC crystals). It is also noted that two ways to break up dipoles are possible: in backward direction (where the self-force assists the breakup), or forward direction (where the

self-force opposes the breakup). For a finite length dipole, the backward break up is obviously easier than the forward one, due to the effects of self forces induced by the two curved dipole arms, as can be seen in Fig. 3(b).

As a final application, we consider dislocation motion in multi-layer anisotropic thin films. It has been experimentally shown that the strength of multilayer thin films is increased as the layer thickness is decreased, and that maximum strength is achieved for layer thickness on the order of 10–50 nm. Recently, Ghoniem and Han [41] developed a new computational method for the simulation of dislocation ensemble interactions with interfaces in anisotropic, nanolaminate superlattices. Earlier techniques in this area use cumbersome and inaccurate numerical resolution by superposition of a regular elastic field obtained from a finite element, boundary element, surface dislocation or point force distributions to determine the interaction forces between 3D dislocation loops and interfaces. The method developed by Ghoniem and Han [41] utilizes two-dimensional Fourier Transforms to solve the full elasticity problem in the direction transverse to interfaces, and then by numerical inversion, obtain the solution for 3D dislocation loops of arbitrary complex geometry. Figure 4 shows a comparison between the numerical simulations (stars) for the critical yield strength of a Cu/Ni superlattice, compared to Freund's analytical solution (red solid line) and the experimental data of the Los Alamos group (solid triangles). The saturation of the nanolayered system strength (and hardness) with a nanolayer thickness less than 10–50 nm is a result of dislocations overcoming the interface Koehler barrier and loss of dislocation confinement within the soft Cu layer.

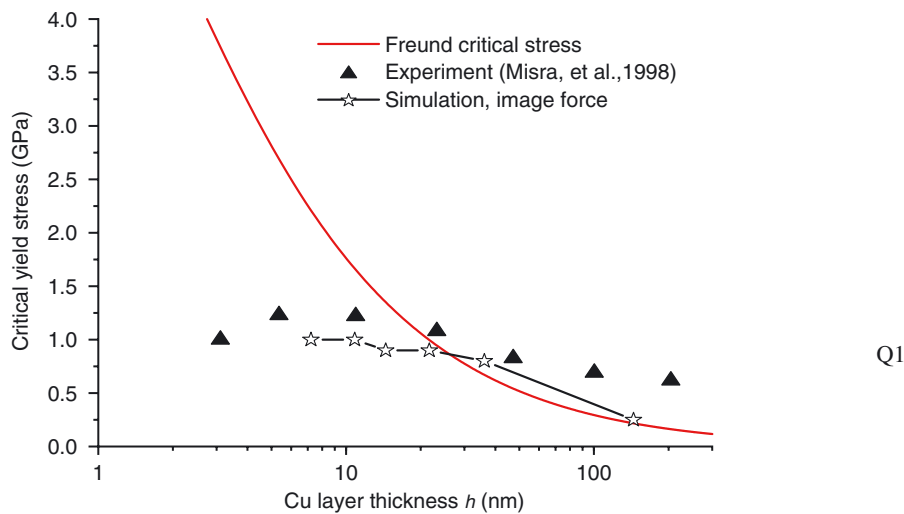


Figure 4. Dependence of a Cu/Ni superlattice strength on the thickness of the Cu layer [41].

## 7. Future Outlook

As a result of increased computing power, new mathematical formulations, and more advanced computational methodologies, tremendous progress in modeling the evolution of complex 3D dislocation ensembles has been recently realized. The appeal of computational dislocation dynamics lies in the fact that it offers the promise of predicting the dislocation microstructure evolution without *ad hoc* assumptions, and on sound physical grounds. At this stage of development, many physically-observed features of plasticity and fracture at the nano- and micro-scales have been faithfully reproduced by computer simulations. Moreover, computer simulations of the mechanical properties of thin films are at an advanced stage now that they could be predictive without ambiguous assumptions. Such simulations may become very soon standard and readily available for *materials design*, even before experiments are performed.

On the other hand, modeling the constitutive behavior of polycrystalline metals and alloys with DD computer simulations is still evolving and will require significant additional developments of new methodologies. With continued interest by the scientific community in achieving this goal, future efforts may well lead to new generations of software, capable of materials design for prescribed (within physical constraints) strength and ductility targets.

## Acknowledgments

Research is supported by the US National Science Foundation (NSF), grant #DMR-0113555, and the Air Force Office of Scientific Research (AFOSR), grant #F49620-03-1-0031 at UCLA.

## References

- [1] H. Mughrabi, "Dislocation wall and cell structures and long-range internal-stresses in deformed metal crystals," *Acta Met.*, 31, 1367, 1983.
- [2] H. Mughrabi, "A 2-parameter description of heterogeneous dislocation distributions in deformed metal crystals," *Mat. Sci. & Eng.*, 85, 15, 1987.
- [3] R. Amodeo and N.M. Ghoniem, "A review of experimental observations and theoretical models of dislocation cells," *Res. Mech.*, 23, 137, 1988.
- [4] J. Lepinoux and L.P. Kubin, "The dynamic organization of dislocation structures: a simulation," *Scripta Met.*, 21(6), 833, 1987.
- [5] N.M. Ghoniem and R.J. Amodeo, "Computer simulation of dislocation pattern formation," *Sol. St. Phen.*, 3&4, 377, 1988.
- [6] A.N. Guluoglu, D.J. Srolovitz, R. LeSar, and R.S. Lomdahl, "Dislocation distributions in two dimensions," *Scripta Met.*, 23, 1347, 1989.

- [7] N.M. Ghoniem and R.J. Amodeo, "Numerical simulation of dislocation patterns during plastic deformation," In: D. Walgraef and N. Ghoniem (eds.), *Patterns, Defects and Material Instabilities*, Kluwer Academic Publishers, Dordrecht, p. 303, 1990.
- [8] R.J. Amodeo and N.M. Ghoniem, "Dislocation dynamics I: a proposed methodology for deformation micromechanics," *Phys. Rev.*, 41, 6958, 1990a.
- [9] R.J. Amodeo and N.M. Ghoniem, "Dislocation dynamics II: applications to the formation of persistent slip bands, planar arrays, and dislocation cells," *Phys. Rev.*, 41, 6968, 1990b.
- [10] L.P. Kubin, G. Canova, M. Condat, B. Devincre, V. Pontikis, and Y. Brechet, "Dislocation microstructures and plastic flow: a 3D simulation," *Diffusion and Defect Data—Solid State Data, Part B (Solid State Phenomena)*, 23–24, 455, 1992.
- [11] A. Moulin, M. Condat, and L.P. Kubin, "Simulation of frank-read sources in silicon," *Acta Mater.*, 45(6), 2339–2348, 1997.
- [12] J.P. Hirth, M. Rhee, and H. Zbib, "Modeling of deformation by a 3D simulation of multi pole, curved dislocations," *J. Comp.-Aided Mat. Des.*, 3, 164, 1996.
- [13] R.M. Zbib, M. Rhee, and J.P. Hirth, "On plastic deformation and the dynamics of 3D dislocations," *Int. J. Mech. Sci.*, 40(2–3), 113, 1998.
- [14] K.V. Schwarz and J. Tersoff, "Interaction of threading and misfit dislocations in a strained epitaxial layer," *Appl. Phys. Lett.*, 69(9), 1220, 1996.
- [15] K.W. Schwarz, "Interaction of dislocations on crossed glide planes in a strained epitaxial layer," *Phys. Rev. Lett.*, 78(25), 4785, 1997.
- [16] L.M. Brown, "A proof of lothe's theorem," *Phil. Mag.*, 15, 363–370, 1967.
- [17] A.G. Khachaturyan, "The science of alloys for the 21st century: a hume-rothery symposium celebration," In: E. Turchi and a. G.A. Shull, R.D. (eds.), *Proc. Symp. TMS*, TMS, 2000.
- [18] Y.U. Wang, Y.M. Jin, A.M. Cuitino, and A.G. Khachaturyan, "Presented at the international conference, *Dislocations 2000*, the National Institute of Standards and Technology," Gaithersburg, p. 107, 2000.
- [19] Y. Wang, Y. Jin, A.M. Cuitino, and A.G. Khachaturyan, "Nanoscale phase field microelasticity theory of dislocations: model and 3D simulations," *Acta Mat.*, 49, 1847, 2001.
- [20] D. Walgraef and C. Aifantis, "On the formation and stability of dislocation patterns. I. one-dimensional considerations," *Int. J. Engg. Sci.*, 23(12), 1351–1358, 1985.
- [21] J. Kratochvil and N. Saxlova, "Sweeping mechanism of dislocation pattern-formation," *Scripta Metall. Mater.*, 26, 113–116, 1992.
- [22] P. Hähner, K. Bay, and M. Zaiser, "Fractal dislocation patterning during plastic deformation," *Phys. Rev. Lett.*, 81(12), 2470, 1998.
- [23] M. Zaiser, M. Avlonitis, and E.C. Aifantis, "Stochastic and deterministic aspects of strain localization during cyclic plastic deformation," *Acta Mat.*, 46(12), 4143, 1998.
- [24] A. El-Azab, "Statistical mechanics treatment of the evolution of dislocation distributions in single crystals," *Phys. Rev. B*, 61, 11956–11966, 2000.
- [25] N.M. Ghoniem, S.-H. Tong, and L.Z. Sun, "Parametric dislocation dynamics: a thermodynamics-based approach to investigations of mesoscopic plastic deformation," *Phys. Rev.*, 61(2), 913–927, 2000.
- [26] R. deWit, "The continuum theory of stationary dislocations," In: F. Seitz and D. Turnbull (eds.), *Sol. State Phys.*, 10, Academic Press, 1960.
- [27] N.M. Ghoniem, J. Huang, and Z. Wang, "Affine covariant-contravariant vector forms for the elastic field of parametric dislocations in isotropic crystals," *Phil. Mag. Lett.*, 82(2), 55–63, 2001.

- [28] J. Hirth and J. Lothe, *Theory of Dislocations*, 2nd edn, McGraw–Hill, New York, 1982.
- [29] M.O. Peach and J.S. Koehler, “The forces exerted on dislocations and the stress fields produced by them,” *Phys. Rev.*, 80, 436, 1950.
- [30] N.M. Ghoniem and L.Z. Sun, “Fast sum method for the elastic field of 3-D dislocation ensembles,” *Phys. Rev. B*, 60(1), 128–140, 1999.
- [31] S. Gavazza and D. Barnett, “The self-force on a planar dislocation loop in an anisotropic linear-elastic medium,” *J. Mech. Phys. Solids*, 24, 171–185, 1976.
- [32] R.V. Kukta and L.B. Freund, “Three-dimensional numerical simulation of interacting dislocations in a strained epitaxial surface layer,” In: V. Bulatov, T. Diaz de la Rubia, R. Phillips, E. Kaxiras, and N. Ghoniem (eds.), *Multiscale Modelling of Materials*, Materials Research Society, Boston, Massachusetts, USA, 1998.
- [33] N.M. Ghoniem, “Curved parametric segments for the stress field of 3-D dislocation loops,” *Transactions of ASME. J. Engrg. Mat. & Tech.*, 121(2), 136, 1999.
- Q2 [34] X. Han, N. Ghoniem, and Z. Wang, “Parametric dislocation dynamics of anisotropic crystals,” *Philos. Mag.*, 2003.
- [35] T. Mura, “Continuous distribution of moving dislocations,” *Phil. Mag.*, 8, 843–857, 1963.
- [36] D. Barnett, “The precise evaluation of derivatives of the anisotropic elastic green’s functions,” *Phys. Status Solidi (b)*, 49, 741–748, 1972.
- [37] J. Willis, “The interaction of gas bubbles in an anisotropic elastic solid,” *J. Mech. Phys. Solids*, 23, 129–138, 1975.
- [38] D. Bacon, D. Barnett, and R. Scattergodd, “Anisotropic continuum theory of lattice defects,” In: C.J.M.T. Chalmers, B (ed.), *Progress in Materials Science*, vol. 23, Pergamon Press, Great Britain, pp. 51–262, 1980.
- [39] T. Mura, *Micromechanics of Defects in Solids*, Martinus Nijhoff, Dordrecht, 1987.
- [40] D. Barnett, “The singular nature of the self-stress field of a plane dislocation loop in an anisotropic elastic medium,” *Phys. Status Solidi (a)*, 38, 637–646, 1976.
- Q3 [41] N. Ghoniem and X. Han, “Parametric dislocation dynamics in multilayer thin films,” *7th US National Congress on Computational Mechanics*, 2003.

## **Author Queries**

1. Figure in color.
2. Please provide vol. no. for Ref. [34].
3. Please provide publisher name and place for Ref. [41].